Journal of
Materials Chemistry A

PAPER

View Article Online
View Journal | View Issue

Cite this: *J. Mater. Chem. A*, 2025, **13**, 42056

High-performance plasma doping as an advantageous vacancy engineering approach for the catalytic activation of materials: the case example of hydroxyapatite

Marc Arnau, *[ab] Montserrat Ferré-Abad, [ab] Carlos Alemán *[abc]
and Jordi Sans *[ab]

Received 23rd August 2025
Accepted 29th October 2025

DOI: 10.1039/d5ta06860f

rsc.li/materials-a

Aiming to transition towards sustainable design processes, plasma doping methods have been investigated as ultra-fast and solvent-free alternatives to chemical doping strategies. Despite their advantages, the current state-of-the-art plasma-doped materials present low doping percentages. Consequently, their acceptance as a replacement to conventional methods is still disfavoured. In this work, we propose a change in the paradigm by presenting a new approach termed high-performance plasma doping (HPPD) capable of intensively doping material lattices. To do so, HPPD exploits the higher number of available sites in vacancy-engineered materials for introducing dopants through non-thermal plasma (NTP) treatment. For this purpose, hydroxyapatite (HAp) is presented as a representative case example of successful HPPD. Thus, HAp disks with OH^- lattice vacancies are prepared and treated for short times with NTP. All the HPPD samples are oxygen-doped successfully, displaying conductivity enhancement of up to one order of magnitude. In addition, doping for the entire material bulk is achieved, reaching a doping replacement efficiency of 50%. The proposed mechanism, based on oxygen diffusion through the OH^- HAp columns, is corroborated through density functional theory (DFT) calculations. Results reveal the key role of lattice vacancies as charge imbalances, exercising an electronic pull on reactive gas species. Further assessment of the HPPD HAp is done through catalytic CO_2 conversion reactions. Thus, the synthesis of C1–C3 products (including ethanol and formic acid, among others) from CO_2 under mild conditions (150 °C and 6 bar of CO_2) is achieved, realizing a total yield of 537.85 ± 3.40 μmol $g_c{}^{-1}$. Finally, the implications of HPPD and its extension towards other materials are discussed and highlighted by performing a state-of-the-art comparison.

1. Introduction

Non-thermal plasma (NTP) technology has become the flagship for the sustainable design of advanced materials standing out for its potential as an ultra-fast and solvent-free technique.[1–3] Its main strength resides in the high degree of customization that is obtained through experimental parameter tuning (*e.g.*, power, atmosphere, pressure and time), rendering vast application possibilities for coating, etching and functionalization of materials.[4–7] Especially, the scientific community has exploited this strategy to assemble next-generation catalysts or restructure the current ones at the nanoscale level. As a result, several synergistic effects for the enhancement of catalytic performance have been achieved.[8–10] For instance, NTP technology is currently being employed for improving catalyst adhesion or promoting favourable electrostatic interactions between the support and the catalytically active part.[11–13] Furthermore, through specific reagent selection, *in situ* synthesis of transition-metal phosphides,[14] composite heterostructures[15] or even nanoparticles[16] have been reported. Consequently, NTP also offers a significant simplification of the chemical fabrication processes and their associated carbon footprint.

Nonetheless, the most promising feature of NTP technology applied to the nano-design of catalysts is its capability for generating surface defects (*i.e.*, atomic vacancies) and/or doping crystal lattices. Such strategies have been intensively used for the generation of binding sites, customization of the selectivity, and/or enhancing the overall photo-/electro-catalytic performance.[17–20] For example, plasma-activated gas species generate atomic vacancies through ion–catalyst collisions, boosting physicochemical properties such as surface reactivity,

---

[a] IMEM-BRT Group, Departament d'Enginyeria Química, EEBE, Universitat Politécnica de Catalunya – BarcelonaTech, C/Eduard Maristany, 10-14, 08019, Barcelona, Spain. E-mail: jordi.sans.mila@upc.edu

[b] Barcelona Research Center in Multiscale Science and Engineering, Universitat Politècnica de Catalunya – BarcelonaTech, 08930 Barcelona, Spain

[c] Institute for Bioengineering of Catalonia (IBEC), The Barcelona Institute of Science and Technology, Baldiri Reixac 10-12, 08028 Barcelona, Spain

electronic conductivity and light absorption, as reported by Zhang *et al.*[21] and Wang *et al.*[22] Besides, depending on the NTP atmosphere used (*e.g.*, air, N_2 or Ar), catalyst doping through uncontrolled atomic substitution has also been achieved, obtaining efficient electrocatalysts for the hydrogen[23] and oxygen[24] evolution reactions (HER and ORR, respectively). However, despite the feasibility of the NTP processes, the reported vacancies and substitutional doping percentages/molar ratios remain low compared to those achieved in conventional strategies.[25] The reduced momentum of NTP ions compared with electrons results in low-energy collisions and consequently a poor chance of atomic substitution (mainly occurring at the interface of the material). Certainly, such low efficiencies contribute to the relegation of NTP technology below chemical doping methods. In any case, considering that NTP enables material modification without compromising crystal lattices (*i.e.*, avoiding heating side effects, as in thermal plasmas), besides being a sustainable strategy for nanoscale design, it is worth revisiting this technology as an alternative technique for atomic doping.

Since the limiting steps are perceived as: (1) the generation of structural vacancies offering favourable sites for substitution/incorporation of the dopants and (2) low bulk doping efficiencies, the aim of this work is to report and establish for the first time the plasma-assisted-bulk-doping of a previously vacancy-engineered material. Because of the higher doping yields at both the surface and bulk, and the low energetic and temporal costs, this procedure will be referred to as High-Performance Plasma Doping (HPPD).

To illustrate the scientific fundamentals and potential of HPPD, hydroxyapatite ($Ca_5(PO_4)_3OH$, HAp) was selected as a case example due to both its vacancy generation feasibility through thermal stimulation treatments and its green nature. Thus, HAp is presented as a great candidate to fully exploit the advantages of HPPD for the challenging development of new sustainable technologies. More specifically, HAp is a highly abundant calcium phosphate salt mostly found in bone tissues, which has been thoroughly studied as a scaffold for tissue regeneration,[26,27] an adsorbent for water purification[28,29] and as a green catalyst for environmental remediation.[30–32] Focusing on its catalytic applications, the intrinsically poor conductivity of HAp renders the sole usage of the ceramic ineffective,[33] forcing the employment of thermal treatments or substitutional doping strategies to enhance its catalytic activity.[34–39] However, the complexity and time costs required to conduct most of these synthesis processes undermine the benefits arising from the synergies in the assembled systems. Furthermore, the complexities of such processes reduce their scalability for future industrial implementation. Nonetheless, refining the electrical properties of HAp remains a topic of great interest, as it has consistently led to significant improvements in all the aforementioned fields. In this sense, it is worth highlighting the use of permanently polarized HAp (p-HAp), achieved through the application of a thermal stimulated polarization (TSP) treatment,[30,35] as it relies only on lattice engineering customization, avoiding the introduction of metallic dopants, thus maximising the biocompatibility and green nature of HAp.

In this work, we prove the feasibility of oxygen HPPD in HAp disks with previously generated hydroxyl group (OH^-) lattice vacancies, demonstrating its potential for achieving surface and bulk oxygen doping while being an ultra-fast and sustainable technique compared to conventional chemical doping methods. In order to do so, HAp disks were calcined at 1000 °C, which generated structural OH^- vacancies, and later treated with NTP under different gas atmospheres (100% O_2, 50/50% O_2/N_2 and 100% N_2). All samples were analysed by Raman spectroscopy and X-ray diffraction (XRD), ensuring no structural phase or chemical alterations were induced during the NTP doping. The direct effects of the treatment were experimentally observed and quantified *via* X-ray photoelectron spectroscopy (XPS) and electrochemical impedance spectroscopy (EIS), and the mechanism behind the ion diffusion and stabilisation of the oxygen dopants into the HAp bulk was elucidated by employing density functional theory (DFT) calculations.

HPPD can be ultimately seen as a refined two-step lattice engineering process involving (1) vacancy engineering and (2) NTP treatment. Therefore, it strongly relies on the "starting" lattice structure of the material before the application of NTP. In this sense, HAp presents a set of unique structural features rendering it a great case example for HPPD. More specifically, HAp offers a wide range of tuneable properties, going from vacancy generation and ion-exchange on several crystalline sites, to the control of the position and proton transference of the OH^- groups arranged in columns along the *c*-axis (see the Discussion for more details). For this reason, p-HAp[30,35] has also been considered as the first step (*i.e.*, a specific kind of vacancy-engineered HAp) to understand HPPD processes, limitations, and potential synergies in sterically charged materials. To highlight the features of the resulting structure, oxygen-doped HAp-based systems have been benchmarked through CO_2 fixation reactions under mild conditions, enabling catalytic performance quantification among the samples prepared in this work. Finally, a brief comparison of state-of-the-art catalyst doping strategies with respect to the present one is presented, revealing insights into the advantages of HPPD and future challenges.

2. Experimental methods

Extended details concerning materials used, HAp synthesis, sample preparation, and characterization techniques and specifications can be found in the SI. Aiming to generate physically uniform samples, HAp disk-shaped pellets were prepared and subjected to one of two thermal treatments: a sintering (1000 °C) or a thermal stimulated polarization (TSP) process (500 V at 1000 °C), herein referred to as s-HAp (*i.e.* sintered HAp) and p-HAp, respectively. Briefly, the TSP treatment is carried out between two stainless steel electrodes (AISI 304) connected by platinum cables to a voltage power supply. A stable continuous voltage supply of 500 V is applied during the treatment at 1000 °C for 1 hour. An initial ramp of 15 °C min^{-1} is applied. At the end of the treatment, samples are left to cool overnight. During both the ramp and cooling steps, the voltage source is maintained at 500 V (see the rest of the details in the SI). Afterwards, the samples were treated by means of a Zepto low-pressure plasma (Fig. S1) from Diener Electronic GmbH Co. (Germany) with an output power of 13.56 MHz (200 W, radio frequency discharge) under different gas atmospheres, 100% O_2 (s-HAp/O or p-HAp/O), 100% N_2 (s-HAp/N or p-HAp/N) and 50/50% v/v O_2/N_2 (s-HAp/ON or p-HAp/ON) for both sintered and polarized HAp disks.

Lattice structural studies were performed through Raman, XRD, and XPS analyses, enabling observation of crystal lattice modifications upon the application of treatment, besides the vacancies and doping quantification. Electrical conductivity changes were studied using EIS, ensuring a proper study of the surface and bulk doping effects. DFT calculations were employed to elucidate the mechanism behind the ionized species diffusion through Nudge Elastic Band (NEB) theory. Plasma-doped sample benchmarking was carried out by means of carbon capture and conversion batch reactions under mild conditions (150 °C, 6 bar CO_2, 40 mL of deionized water for 24 h). Accordingly, the products collected, found in the aqueous supernatant and adsorbed in the catalyst, were analysed by ^{1}H-NMR spectroscopy. A comparison with state-of-the-art plasma doping strategies was performed according to two factors: (1) energy employed to perform the plasma doping, taking into account time and equipment power, and (2) percentage of doping replacement achieved, understood as the ratio between the ionic species substituted and the available substituting sites.

3. Results and discussion

3.1 Lattice-engineering in HAp as the first step to HPPD: vacancy generation and electro-thermal reorientation

As noted above, two initial HAp lattice-engineered states are considered for the application of the NTP treatment: (1) HAp containing OH^- vacancies, and (2) p-HAp. Because the ultimate objective of HPPD is to enhance the catalytic activity of HAp by customizing its electrical properties, special attention is put on determining possible structural distortions and new lattice arrangements, as they are closely related to electronic and ionic transport phenomena.[30] Below presented are the most relevant features of both HAp states. After synthesizing HAp, ensuring the generation of considerable numbers of vacancies in the HAp crystal lattice without compromising its structural stability was deemed crucial for maximizing the doping candidate sites. HAp is mostly synthesized and/or naturally encountered in a hexagonal crystal phase ($P6_3/m$ space group symmetry), consisting of Ca^{2+} ions withholding tetrahedral phosphate groups (PO_4^{3-}) while being spaced by OH^- group columns. Such OH^- species are non-directionally distributed along the lattice columns, compensating the steric charge effects arising from the lattice. Furthermore, the local configuration of PO_4^{3-} enables a distinction between two spatially distributed calcium types, hereinafter referred to as Ca I and Ca II, see Fig. 1a. Although noteworthy works have reported substitution or vacancy generation for Ca and P ions, the resulting materials usually differ greatly from the stoichiometric HAp (~1.67 Ca/P).[40–42] Hence, liberating OH^- groups from the HAp crystal lattice has become the most adopted vacancy engineering strategy for this ceramic,[30,43–47] being extremely feasible due to the capacity of HAp to induce OH^- vacancies upon application of a high-temperature dehydration treatment.[48,49]

In this work, the generation of OH^- defects in sintered HAp (s-HAp) disks at 1000 °C has been validated and quantified through Raman spectroscopy and XRD analysis (experimental details can be found in the ESI). In Fig. 1b, $\nu_1 = 400-480$, $\nu_2 = 570-625$, $\nu_3 = 965$, $\nu_4 = 1020-1095$, and $\nu_5 = 3574$ cm^{-1} Raman active modes, attributed to phosphate bending and symmetric/asymmetric stretching vibrations, are detected for all samples, confirming the proper synthesis of HAp.[48] The successful vacancy generation was confirmed by considering the normalized peak areas of the stretching vibration mode ν-OH at 3575 cm^{-1} (Fig. 1b). As expected, a decrease in the area from 0.265 A.U. (as-prepared HAp) to 0.171 A.U. (s-HAp) is observed, which is consistent with the literature.[48,49] Furthermore, the HAp hexagonal crystallographic phase was identified in all samples through XRD diffractograms (Fig. 1c), with the characteristic HAp reflections corresponding to (002), (211), (112), (300), (202) and (310) crystallographic planes appearing at $2\theta =$ 25.9°, 31.7°, 32.1°, 32.8°, 34.0° and 39.8°, respectively (JCPDS card number 9-0077). Moreover, a structural refinement for the s-HAp samples is achieved, reaching a crystallinity (χ_c; see SI) of 0.95 as compared to 0.66 for HAp. Overall, such results are advantageous since they ensure the following: (1) the presence of non-refined calcium phosphate phases, which could introduce cell distortions, is avoided and (2) the generation of OH^- vacancies does not compromise HAp's structural integrity.

On the other hand, to obtain permanently polarized samples, the remaining OH^- groups in s-HAp are rearranged in the *z*-axis direction through the TSP treatment, resulting in conductively enhanced p-HAp (Fig. 1a). As reported by Sans *et al.*,[48] direct observations of OH^- reorientation can only be detected through normalized peak area changes for the ν-OH mode, mainly related to a less efficient energy transfer between unpolarized light and directionally oriented OH^- dipoles. Accordingly, p-HAp shows a smaller area (0.125 A.U.) compared to s-HAp. Moreover, the presence of hydroxyl-stabilized brushite, a surface metastable calcium phosphate phase (detected through the 797 and 882 cm^{-1} Raman active modes), is also reported to be an indicator of successful polarization.[48] Despite undergoing a partial lattice rearrangement, the XRD reflections and the crystallinity index (*i.e.* $\chi_c = 0.96$) are maintained (or even further refined) for both p-HAp and s-HAp, confirming that no structural damage occurred during the treatment. Additional observation of the surface brushite phase through Wide-Angle X-ray Diffraction (WAXD) can be seen in Fig. S2.

Ultimately, the authors find that giving a comprehensive schematic picture for the s-HAp and p-HAp samples is of utmost importance, ensuring correct system understanding before the discussion in the following sections. Accordingly, in Fig. 1a and d, both assembled systems with their characteristic lattice features can be observed. As mentioned, both approaches present the same number of generated vacancies. However, p-HAp is differentiated by the specific orientation of the OH^-

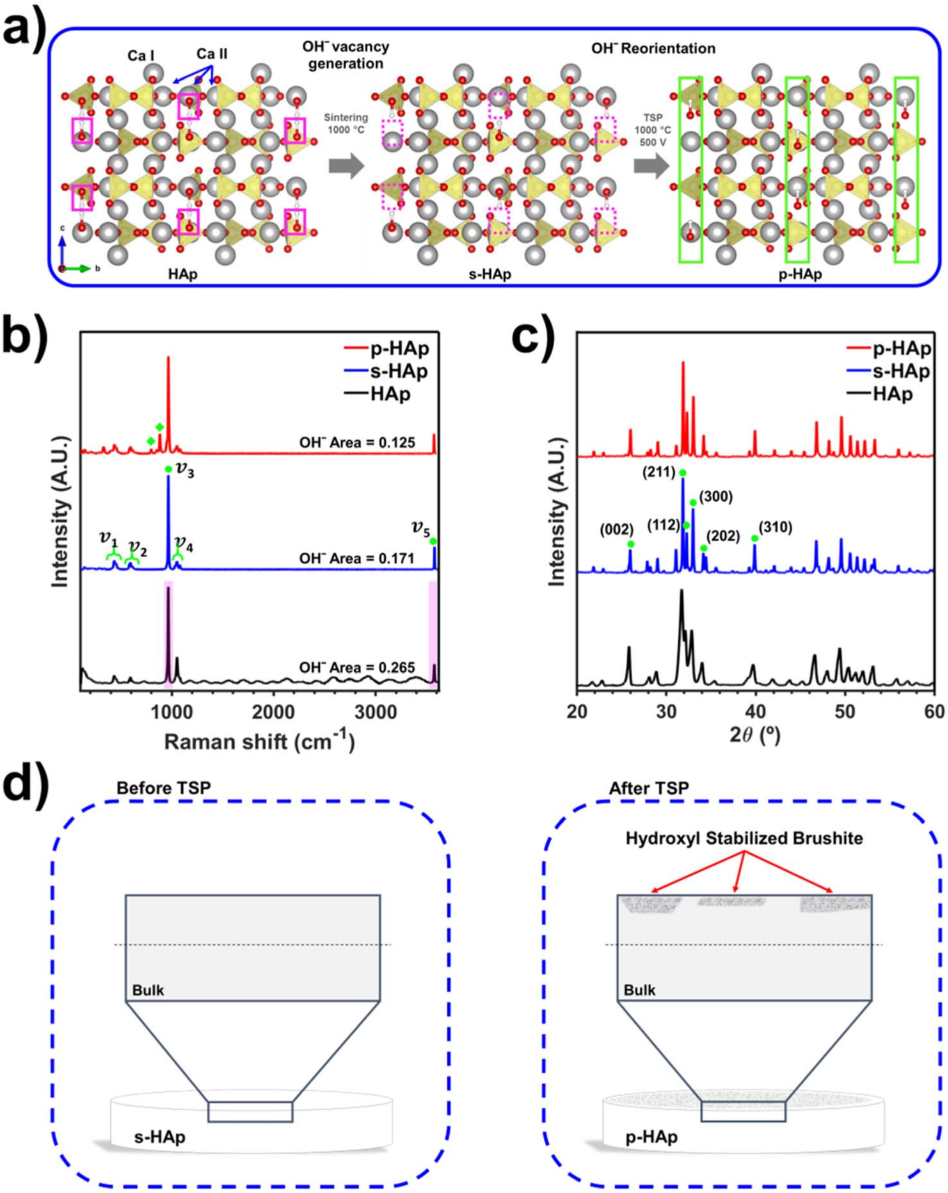

Fig. 1 a) Scheme highlighting the main atomic features of HAp, s-HAp and p-HAp. (b) Raman spectra obtained for the as-prepared HAp, s-HAp and p-HAp samples. Main characteristic modes for HAp are marked in green in s-HAp. Green diamonds mark hydroxyl-stabilized brushite. Normalized OH^- peak area with respect to 965 cm^{-1} active mode area is also displayed. (c) XRD diffractograms for the same three samples with markings on the typical reflections of HAp. (d) Macroscopic attributes of the s-HAp and p-HAp disks.

groups (shown in Fig. 1a) and the detection of brushite surface clusters (Fig. 1d). Indeed, both systems possess identical charge imbalance (*i.e.*, vacancies); nonetheless, the directional alignment of OH^- groups in p-HAp enables charge delocalization through its grain boundaries, promoting surface charge accumulation.[48]

3.2 Plasma doping effects in vacancy-engineered hydroxyapatite

As mentioned in the Experimental methods section, NTP treatment with different plasma gases was applied to s-HAp disks, labelled as s-HAp/O, s-HAp/ON, and s-HAp/N for 100% O_2, 50/50% O_2/N_2, and 100% N_2, respectively. SEM images (Fig. S3) and EDS maps (Fig. S4) reveal a homogeneous distribution of species, without any significant changes in the morphology before and after the NTP treatment. This was an expected result due to the nature of the plasma set-up used (*i.e.*, non-thermal and non-atmospheric). For this reason, the specific surface area measured by BET (3.28 ± 0.06 m^2 g^{-1}, Fig. S5) can be assumed to be maintained for all the samples, and does not play a role in the resulting enhanced electrochemical and catalytic properties. Despite the fact that NTP results in lower energy plasma-sample particle collisions as compared to the more aggressive thermal plasmas, minor amounts of surface lattice distortions are still detected in the Raman analyses. As seen in the inset of Fig. 2a, the bands at

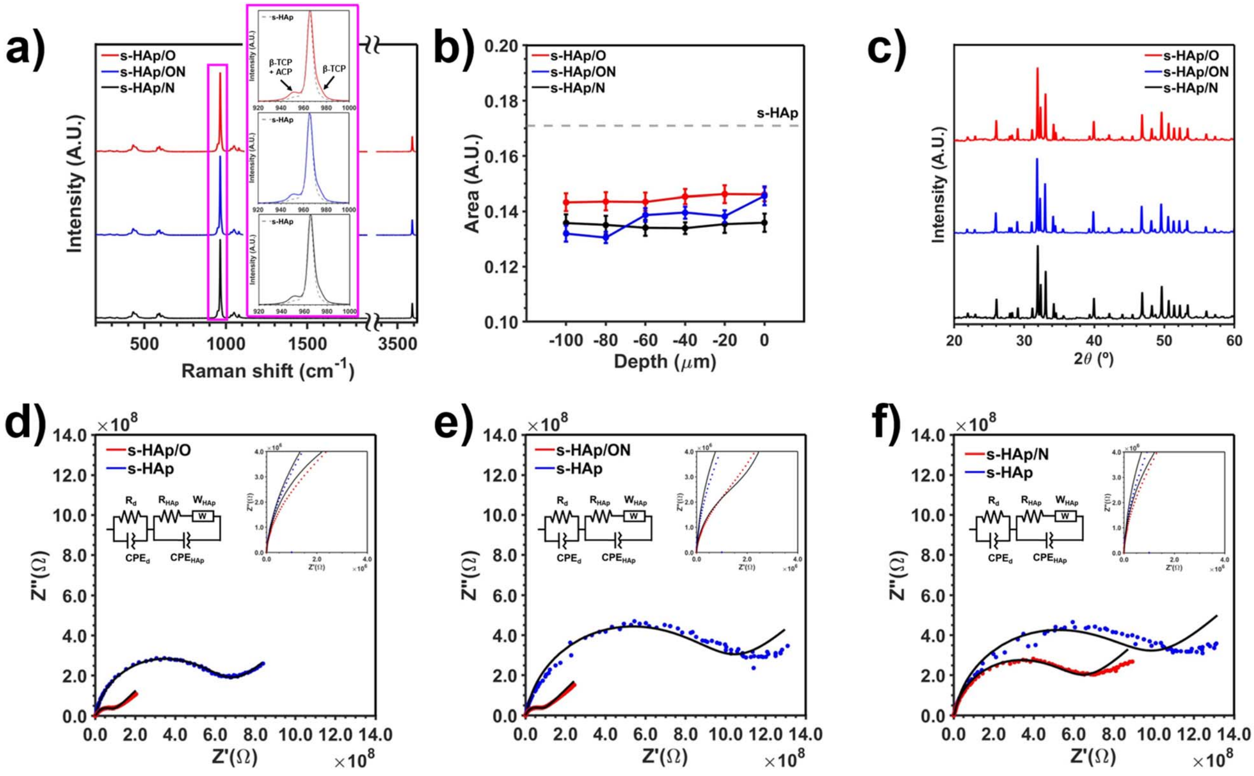

Fig. 2 (a) Raman spectra of the s-HAp samples after NTP treatment. Arising calcium phosphate species are displayed through the pink solid line in the inset. (b) Normalized peak area for the OH$^-$ Raman active mode measured at different sample depths. Grey dashed line marks the surface value for non-treated s-HAp. (c) XRD diffractograms for all the plasma-treated samples. (d)–(f) Nyquist plots for s-HAp/O, s-HAp/ON, and s-HAp/N, respectively. Every plot displays the sample prior to (s-HAp) and after (s-HAp/X) the treatment, enabling direct comparison between them while avoiding the electrochemical response experimental variability associated with the preparation of each sample.

~950 and ~975 cm^{-1} are attributed to a mixture of β-tricalcium phosphate ($Ca_3(PO_4)_2$; β-TCP) and amorphous calcium phosphate (ACP), which were not previously observed in the s-HAp samples.[49] Nonetheless, 2D high-resolution (HR) Raman surface maps display <9% peak intensity ratio (I_{950}/I_{965}) for all samples (Fig. S6). For this reason, in this study, the contribution of such distortions has been assumed to be minimal. Since no significant evidence of successful doping is detected on the surface of the samples, in-depth Raman measurements were carried out, mainly focusing on the area evolution of the OH$^-$ active vibration mode. In all cases shown in Fig. 2b, an average 15–22% decrease for the normalized OH$^-$ areas is observed with respect to s-HAp, independent of the depth. Indeed, detecting such an area decrease at the surfaces can be partially associated with the formation of the aforementioned distortions (*i.e.*, β-TCP does not contain OH$^-$ groups). However, noticing that in Fig. S7 the β-TCP contribution decreases moderately inside the bulk, the sustained smaller area observed could be attributed to the diffusion of NTP reactive gas species through the OH$^-$ columns, which overshadows their signal. In this sense, the fact that the NTP reactive gas species are specifically allocated in the OH$^-$ crystallographic sites (rather than random sites in the lattice) implies that no bulk structural damage should be detected. Accordingly, the XRD diffractograms shown in Fig. 2c, apart from minor crystallinity changes, show neither new crystalline structures nor a reduction of the crystallinity index (χ_c = 0.95, 0.97 and 0.94 for s-HAp/O, s-HAp/ON and s-HAp/N; respectively). Overall, these first results suggest that a general bulk doping occurs after the application of the NTP treatment.

To further support such a significant conclusion, EIS (Fig. 2d–f) analyses were carried out. Accordingly, EIS measurements were performed before and after the different NTP treatments, enabling direct observation of the resulting electrical response of the whole system (*i.e.*, bulk and interphase). As can be observed in the Nyquist plots shown in Fig. 2d–f, an outstanding conductivity improvement is achieved for all samples; precisely, increases of one order of magnitude for the samples treated with plasma oxygen. It must be noted that all electrical responses modelled using the electric equivalent circuits (EEC) display two behaviours: one at high frequencies and one at low frequencies. More specifically, both features have been associated with the β-TCP surface distortions (their contribution in the EEC model is labelled as "d") and the HAp bulk, respectively. As seen in Table 1, the fitted parameters accounting for distortions remain similar after the NTP application (which is in agreement with the structural observation discussed above), with the doped bulk being the sole cause for the modification in the conductive behaviour. Specifically, when considering all HAp bulk circuit parameters, only the bulk resistance (R_{HAp}) experiences significant variation.

Table 1 Equivalent electric circuit parameters from the fitted data obtained in the EIS measurements. Subscript d refers to distortions (*i.e.*, non-HAp phases), while HAp subscript refers to the bulk of the s-HAp samples

EEC model	s-HAp	s-HAp/O	s-HAp/ON	s-HAp/N
R_d (MΩ cm^{-2})	3.55	4.05	1.54	2.89
Error (%)	8.57	8.05	6.25	6.91
CPE$_d$ (pF cm^{-2} sn^{-1})	18.38	20.08	16.36	14.02
Error (%)	16.29	12.51	11.58	13.21
n_d	1.00	0.97	1.00	1.00
Error (%)	1.81	1.55	1.25	1.43
R_{HAp} (MΩ cm^{-2})	618.94	59.77	58.18	441.67
Error (%)	1.60	3.16	1.65	1.48
CPE$_{HAp}$ (pF cm^{-2} sn^{-1})	40.65	115.91	67.42	43.48
Error (%)	2.86	9.23	4.92	3.01
n_{HAp}	0.91	0.88	0.90	0.91
Error (%)	0.56	1.91	0.84	0.57
W_{HAp} (nF cm^{-2} s$^{-1/2}$)	1.99	5.44	4.00	2.20
Error (%)	4.73	2.66	1.31	3.82

For instance, R_{HAp} decreases from 618.94 MΩ cm^{-2} to 59.77 MΩ cm^{-2} in s-HAp/O, confirming that a general doping has occurred, lowering the HAp bulk resistance. Such enhancement in the electrical properties of HAp falls in the same range of p-HAp (*i.e.* $R_{p\text{-}HAp} = 10.34$ MΩ cm^{-2}, see the discussion in Section 3.4 Plasma doping effects in polarized hydroxyapatite). Hence, we successfully report an alternative method for customizing the electrical properties of HAp, avoiding the introduction of metallic particles/dopants. Besides, the presence of oxygen in the NTP treatment appears to be necessary, since a scarce 28% conductivity improvement is obtained for the s-HAp/N, which is in contrast to the 90% achieved in oxygen-rich atmospheres. Overall, three crucial insights can be gained from these results: (1) NTP application results in great conductive enhancement, especially when using oxygen-rich atmospheres. (2) Although some surface distortions are detected in the Raman spectra after the treatment application, the structure of HAp is not compromised, as corroborated by the presented diffractograms. (3) As seen in the EIS, NTP promotes HAp bulk doping. However, since structural variations are not observed in the XRD, the results suggest that the doping process occurs *via* channelled diffusion of reactive gas species, preserving the HAp structure.

XPS analyses were performed to elucidate which atomic species regulate the doping phenomena at the surface. The results are displayed in Fig. 3. Firstly, it is worth mentioning the fact that all peaks in the O 1s, Ca 2p and P 2p regions for the NTP-treated samples are shifted towards lower binding energies with respect to s-HAp (1.4, 0.7 and 0.6 eV, respectively). This energetic lowering is directly related to charge density changes in the vicinity of the HAp species, indicating the presence of p-type dopants in the samples (*i.e.* atoms that generate holes through electron capture from the overall system).[50–52] Although nitrogen and oxygen reactive species were expected to be detected in the N 1s and O 1s XPS regions, surprisingly, only a residual amount of nitrogen species was observed in all samples (Fig. S8), which cannot be associated with doping but rather with adventitious carbon–nitrogen species. In the O 1s region (Fig. 3a), apart from the characteristic HAp oxygen species arising from the double (531.0 eV) and single (529.7 eV) bonded oxygen (O^0 and O^-, respectively) atoms in PO_4^{3-} tetrahedra,[53] a new peak appears at 527.9 eV. As seen in Table 2, the latter oxygen species are observed in all NTP-treated samples but not in the control s-HAp. Therefore, this new peak was associated with oxygen dopant species, hereafter labelled as O-d, confirming the nature of the dopants in the system. Accordingly, the atomic concentration for O-d increases proportionally to the volume percentage of oxygen used in the NTP treatments, from 2.73% (s-HAp/ON) to 5.62% (s-HAp/O). Nevertheless, 1.43% of such species are similarly detected in samples prepared without an oxygen atmosphere, suggesting the possibility that 100% N_2 NTP is also capable of ionizing oxygen atoms from external non-HAp sources and enabling their latter diffusion, thus replicating a similar process as proposed for s-HAp/ON and s-HAp/O. This hypothesis can be corroborated since no new P or Ca species, which would indicate that HAp structure has been compromised, are detected in

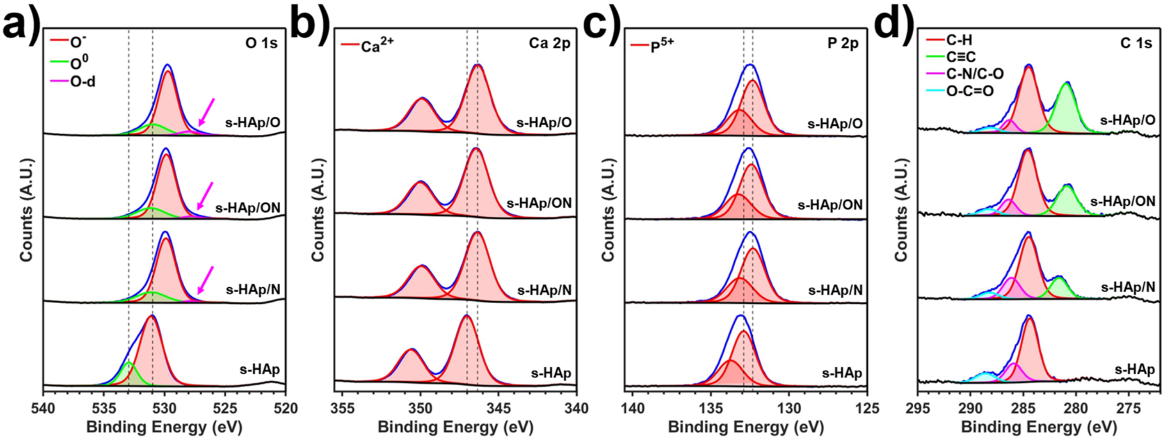

Fig. 3 High-resolution XPS spectra for the O 1s, Ca 2p, P 2p and C 1s regions, (a), (b), (c) and (d), respectively. Grey dashed lines are used as a binding energy shift indicator, facilitating qualitative observation.

Table 2 Atomic concentration (%) of oxygen species detected by XPS in the O 1s region

	O^- (529.7 eV)	O^0 (531.0 eV)	O-d (527.9 eV)
s-HAp	80.03	19.97	0.00
s-HAp/O	75.53	18.86	5.62
s-HAp/ON	77.84	19.43	2.73
s-HAp/N	78.88	19.69	1.43

the P 2p and Ca 2p regions for the s-HAp/N sample (Fig. 3b and c). Therefore, since HAp cannot be considered as the provider for O-d in 100% N_2 NTP conditions, the most probable remaining source was attributed to the adventitious carbon found on the surface of the samples. Certainly, several carbon species were detected in the C 1s region of s-HAp (Fig. 3d), attributed mainly to C–H (284.4 eV) with minor composition of C–N/C–O (285.9 eV) and O–C═O (288.6 eV).[54] After the application of NTP, a re-assembling seems to occur, partially converting the former carbon species into carbides, C≡C (281.0).[55] Actually, the O–C═O concentration decreases from 11.77% in s-HAp to 6.16% in s-HAp/N, being the most plausible origin for the 1.43% O-d detected in s-HAp/N, whereas NTP nitrogen reactive gas species would be acting as an oxygen-liberating agent through carbide formation. Further atomic percentages reflecting the concentration of general atomic and carbon species can be found in Tables S1 and S2. As expected, such a process is less efficient, leading to poorer electrical enhancement, as highlighted by the resulting electrical parameters in Table 1.

To summarize, XPS results further prove that all NTP-treated samples become oxygen-doped. While oxygen atmospheres promote direct oxygen doping, nitrogen reactive species act as cleavage agents, enabling oxygen release from surface adventitious carbon and its latter diffusion. On the whole, all NTP treatments result in outstanding conductivity enhancements, as seen by EIS (Fig. 2d–f and Table 1). However, employing an NTP with an oxygen-rich atmosphere is essential to carry out HPPD successfully. Concerning the doping process efficiency, two key aspects need to be considered prior to the calculation: (1) from the 19 possible oxygen positions in the (001) crystallographic plane for HAp (Scheme S1), only the hydroxyl group vacancy can accept an oxygen ion, since replacing one of the 18 remaining could result in structural distortions, as seen in Fig. 2c. Thus, a theoretical maximum surface doping uptake of ~5.3% has been determined; and (2) as clearly seen in the EEC bulk parameters and indicated through depth Raman studies, the doping is carried out uniformly throughout the bulk, presumably, through diffusion processes. The feasibility of the mechanism derived from such a point is discussed in the section below. Then, considering that 5.62% of O-d are detected for s-HAp/O and a maximum of 5.3% of the surface might act as oxygen attraction points, the surface doping process efficiency would be ~100% for pure O_2 NTP (s-HAp/O) and ~50% for the 50/50 v/v% O_2/N_2 mixture (s-HAp/ON). Thereby, generating OH^- vacancies in the HAp crystal lattice has been proven as a remarkable strategy for intensively doping the material with oxygen atoms, leading the authors to qualify it as HPPD. Further comparison with state-of-the-art doping techniques is discussed in Section 3.5 Catalytic benchmarking of HPPD hydroxyapatite-based composites, evaluating the future perspectives of HPPD.

3.3 Breaking down the mechanism of HPPD

Surface doping was directly observed in XPS analyses, while bulk doping was confirmed through the EIS experimental data. Considering that no structural changes occurred during the NTP treatment, the results suggest the diffusion of oxygen ions throughout the OH^- channels towards the bulk of s-HAp. In order to evaluate the feasibility of the former transport process, DFT calculations were conducted. For that, 1 × 1 × 4 supercells (169 atoms) resembling s-HAp were designed while centering the unit cell on the OH^- column (additional details are provided in the SI). Finally, an exact amount of 50% vacancies were generated and distributed in three different column arrangements Fig. 4a, S9a and S10a, while one oxygen atom was positioned on each column surface vacancy. Given that the main objective behind the theoretical calculations is to demonstrate bulk doping viability by means of oxygen transport, and knowing that 70 possible intermediate states can be generated from each initial column state, the authors decided to model oxygen ion/OH^- movement in the columns according to three assumptions: (1) all oxygen ions or OH^- group movements should be directionally preferred from top to bottom of the column (*z*-axis direction). (2) Species movement should conserve momentum (as in a Newton pendulum). Thus, if a moving species is blocked by another one or more in the column, the latter should continue moving through the column. (3) No groups of more than 3 consecutive species should be formed, since it can be assumed that certain charge neutral zones would appear opposite to highly positive ones (vacancies), resulting in partially ordered regions and, thus, not being entropically favourable.

NEB calculations were performed, enabling bridging intermediate states among the different column types in the supercells to be identified (Fig. 4b). Although activation energy is required in all transitions, the diffusion movement of the oxygen dopant appears to be energetically preferable in almost all cases. However, even though all the systems evolve towards stable states, energy barriers of ~1 eV still need to be overcome in order to confirm the transport mechanism's feasibility. Accordingly, the authors propose a mechanism that facilitates the understanding of the feasibility of such behaviour. DFT calculations were performed to simulate very specific cases without accounting for plasma effects such as electrical sheaths.[56] Considering that s-HAp is positively charged as a consequence of generating OH^- vacancies, and knowing that the NTP steady-state tends to form electrically neutral gas environments despite atomic species ionization,[57] a voltage difference between the NTP gas reactive species (ϕ_1) and the samples (ϕ_2) is expected. This phenomenon should be understood as an electrical field, compensating the whole system (reactive species and sample) potential difference formed through the aforementioned charge imbalance. The proposed

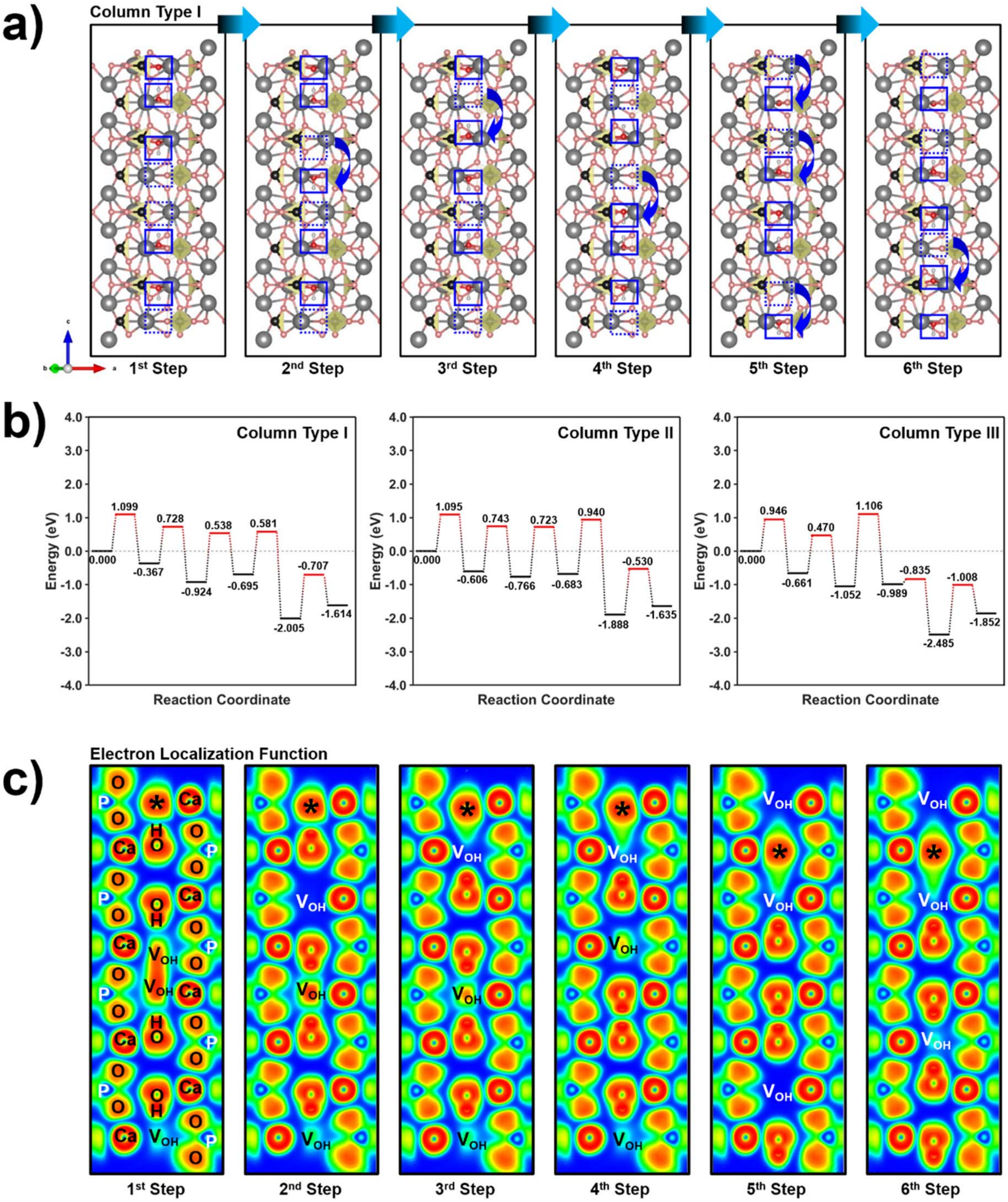

Fig. 4 (a) Scheme in which the column arrangement type I can be observed in the 1st step. The subsequent diffusion steps refer to the intermediate images displaying the hydroxyl groups/dopant transportation through the s-HAp column. Solid line squares mark the species, dashed line squares mark the vacancies, and blue arrows display the movement occurring to reach the present image. Type II and type III columns are displayed in Fig. S9a and S10a, respectively. (b) Nudge elastic band calculations enabling bridging diffusion intermediate steps from an activation energy barrier point of view. Black solid lines mark the initial/final states respectively, while a red colour is used to indicate the transition states. (c) Electron localization function calculated for all the diffusion steps. The $(1\bar{1}0)$ crystallographic plane is displayed. The (110) crystallographic plane is also obtained and can be seen in Fig. S11, enabling further insights into the neighbouring electron effects. Ca, P, and O–H crystallographic positions are highlighted. Furthermore, oxygen dopants and O–H vacancies are marked as * and V_{OH}, respectively.

mechanism is depicted in Scheme 1. The emergence of an electrical field would consequently result in a driving force pulling electrons, which, in turn, would drag ionized nuclei along the way, sustaining the neutral charge gas regime. It is worth mentioning that the principle behind this mechanism resembles that of the TSP process, where a temperature-aided electric field is used as a driving force for inducing crystal lattice changes.

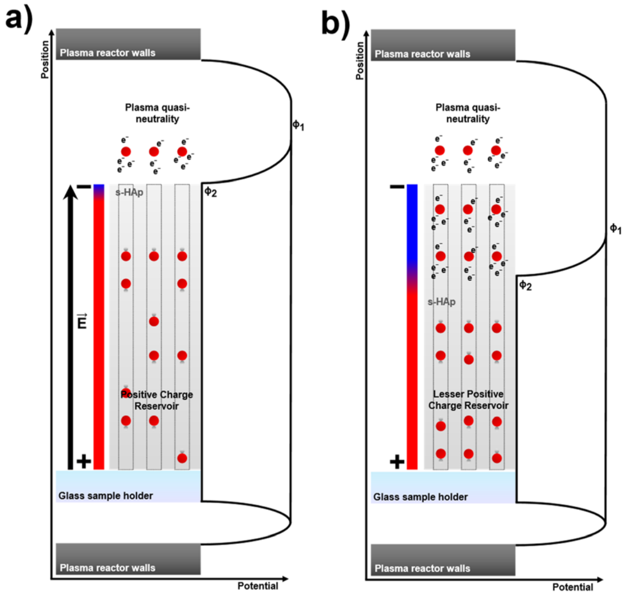

Scheme 1 . (a) and (b) Schemes for initial and mid HPPD on s-HAp, respectively. In (a), s-HAp acts as an infinite positive charge reservoir, attracting electrons, which, in turn, drag positive oxygen ions. In (b), the first two layers are doped, achieving a charge quasi-neutrality (as in the plasma), and hence, the outer plasma potential (ϕ_1) can be assumed to be similar in this first region. ϕ_2 accounts for the sample "inner" potential.

Although no experimental proof can be achieved confirming the former oxygen diffusion mechanism, calculations for the electron localization function (ELF) in the different intermediate states of the columns yielded a highly interesting result. Fig. 4c shows that the ELF for the oxygen dopant (*) in steps 4 to 6 presented an elongated and bulk-oriented shape. Due to proximity to a vacancy (V_{OH}; positively charged region), the electrons from the oxygen dopant are more likely to be localized towards the upper vacancy region. That is, in the simulations, the dopant oxygen experiences an electronic pull towards the bulk even without accounting for a plasma-generated compensating electrical field. This result can also be observed in the ELF distributions displayed in Fig. S9b, S10b and S11. Furthermore, as reported in Kortshagen *et al.*,[56] typical electron temperatures in NTP are measured to be 1–5 eV, reaffirming the possibility of these fermions being the initiators for the proposed mechanism in this section, overcoming the ~1 eV diffusion transport energy barrier.

3.4 Plasma doping effects in permanently polarized hydroxyapatite

Apart from studying plasma doping effects on vacancy-engineered HAp, the polarized version of the ceramic (*i.e.* p-HAp; Fig. 1) has also been studied with the aim of characterizing and reporting the NTP effects arising on it, for the first time. In this sense, the specific orientation of the OH^- groups in the p-HAp is expected to play a different role in the diffusion of the oxygen dopants and, thus, the overall doping. As mentioned, pure O_2, N_2 and 50/50 v/v% O_2/N_2 mixture NTP atmospheres were used to prepare the samples, as described for the s-HAp. A summary of the results obtained during the p-HAp/X study is presented in Fig. 5. In contrast to the s-HAp results, the application of NTP to p-HAp does not result in an outstanding improvement. The EIS results in Fig. 5a were fitted according to the EECs reported elsewhere,[58] which also takes into account the TSP-generated layer of hydroxyl-stabilized brushite, as described in Fig. 1c.

Table 3 shows that the application of NTP does not result in a direct electrical improvement in the p-HAp bulk (R_{HAp}), experiencing ± 1 MΩ cm^{-2} changes. Alternatively, the brushite surface layer resistance (R_B) decreases from 605.50 MΩ cm^{-2} to 218.71 and 185.12 MΩ cm^{-2} for p-HAp/O and p-HAp/N, respectively. Considering that brushite crystals tend to be structurally unstable at ambient conditions,[59] Raman studies were performed to determine whether a plasma-assisted degradation process was occurring on the surface of the samples. However, the acquired spectra, displayed in Fig. 5b, reveal that the brushite characteristic peaks at 797 and 882 cm^{-1} are still detected for the p-HAp/O and p-HAp/N samples, suggesting that surface brushite does not deteriorate. On the other hand, a p-HAp sample with a low amount of brushite was also prepared through tuning the TSP treatment atmosphere,[30,59] and subsequently NTP treated with the mixed atmosphere, resulting in p-HAp/ON. Despite the lower amount of brushite (see the inset of Fig. 5b), only a limited improvement (~48%) in the remaining R_B is detected compared with p-HAp/O or p-HAp/N, while no variations are achieved for the p-HAp resistance (R_{HAp}). These results indicate that, first, p-HAp resists plasma doping despite possessing equal numbers of vacancies as s-HAp; and, second, the surface layer of the brushite seems to accept the reactive gas species and, thus, becomes doped. Furthermore, XRD acquired for the three samples (Fig. 5c) does not reveal significant structural changes besides minor shifts in the HAp crystallographic plane intensities, attributed to fabrication reproducibility.

Finally, to conclude this section, XPS studies were also carried out to obtain further insights on the ruling species for the brushite plasma doping (Fig. 5d–g, Tables S3 and S4). As in the s-HAp/X samples, all regions present a lowering of the binding energy; specifically, 0.7, 0.6 and 0.5 eV for the O 1s, Ca 2p and P 2p regions, respectively. Similar to NTP-doped s-HAp samples, oxygen dopant species are also observed at 529.0 eV (O-d), while new peaks at 527.6 and 525.4 eV, named hereinafter as O-CaP, are attributed to brushite undergoing an oxygen doping process. Unexpectedly, the NTP oxygen doping behaviour in p-HAp samples is completely opposite to that observed in s-HAp. The highest concentration of oxygen-doping species (O-d, O-CaP) is found in the p-HAp/N sample (~13%, Table S5), while carbide species seem to progressively increase their number proportionally to the N_2 atmospheric concentration from 5.15% to 37.99% (Fig. 5g and Table S4). On the whole, the biphasic nature of p-HAp seems to facilitate oxygen doping of the brushite interphase through ionization of adsorbed O═C–O and C–O adventitious carbon species, mediated by nitrogen reactive gas species. However, as highlighted by the EIS studies, O-d cannot diffuse throughout the bulk of the sample, thus

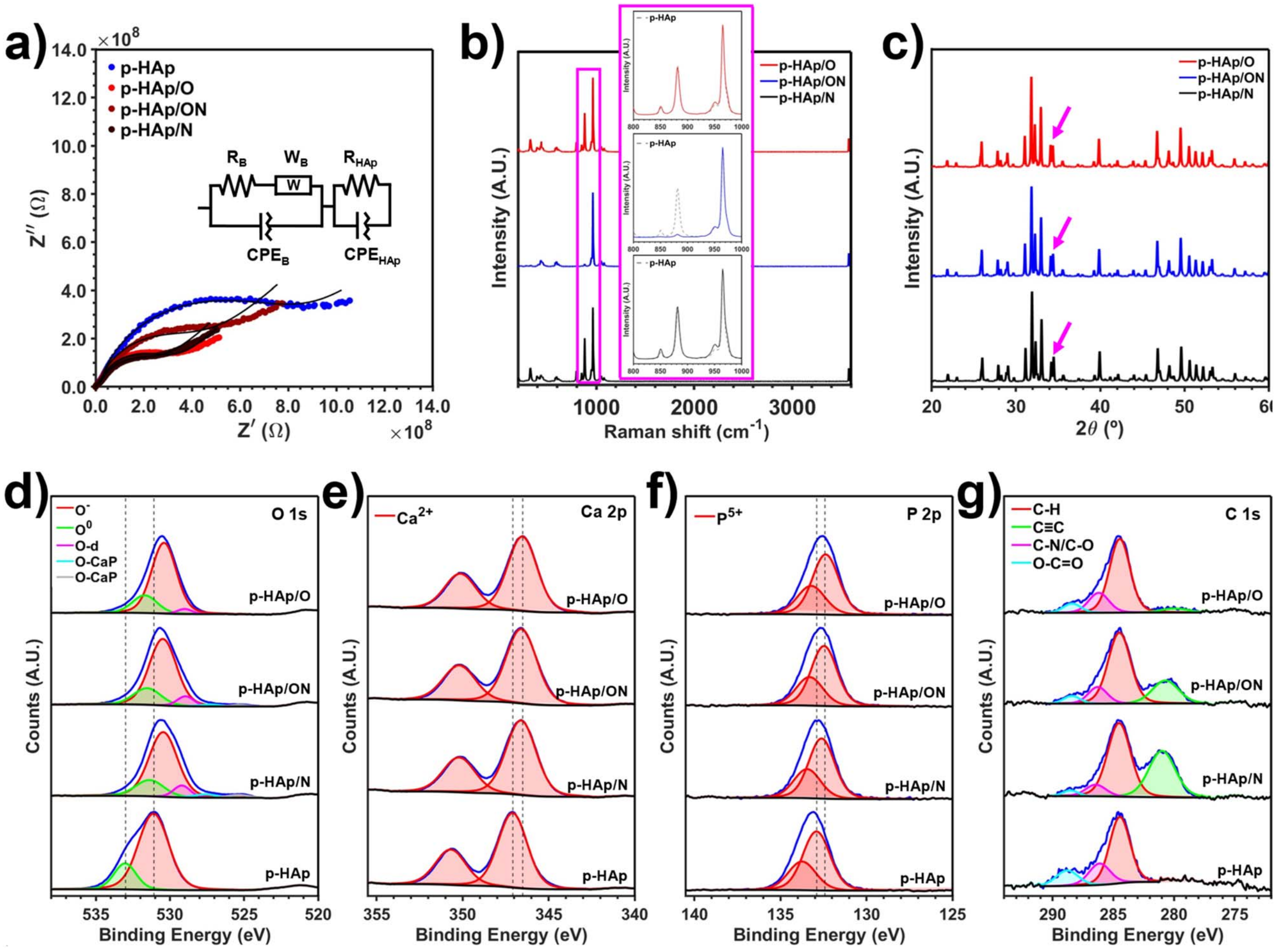

Fig. 5 (a) Nyquist plots for the p-HAp/O, p-HAp/ON and p-HAp/N samples. (b) Raman spectra for the p-HAp samples after NTP treatment. Arising calcium phosphate species are also displayed through the pink solid line in the inset. (c) XRD diffractograms for all the polarized plasma-treated samples. (d)–(g) O 1s, Ca 2p, P 2p and C 1s XPS regions, respectively. Grey dashed lines mark peak shifts between samples.

Table 3 EEC parameters for the p-HAp NTP treated samples. Subscript B is used to identify the brushite electric circuit elements, while the HAp subscript indicates p-HAp ones

EEC model	p-HAp	p-HAp/O	p-HAp/ON	p-HAp/N
R_B (MΩ cm^{-2})	605.50	218.71	310.19	185.12
Error (%)	3.44	3.35	4.28	5.93
CPE$_B$ (pF cm^{-2} sn^{-1})	122.80	117.31	107.13	156.55
Error (%)	4.23	6.76	6.59	11.09
n_B	0.84	0.88	0.88	0.85
Error (%)	1.14	1.61	1.60	2.86
W_B (nF cm^{-2} s$^{-1/2}$)	2.13	2.97	1.71	2.66
Error (%)	8.48	4.51	4.48	4.86
R_{HAp} (MΩ cm^{-2})	10.34	11.08	11.64	12.91
Error (%)	6.49	5.09	6.18	7.87
CPE$_{HAp}$ (pF cm^{-2} sn^{-1})	20.89	13.52	15.72	25.51
Error (%)	11.13	8.28	9.95	8.80
n_{HAp}	0.96	0.97	0.98	0.90
Error (%)	1.42	1.02	1.28	1.30

resulting in low oxygen HPPD. As aforementioned, the p-HAp sample prepared with low brushite content confirms that brushite is not responsible for obstructing the O-d diffusion, as the bulk electrical resistance of p-HAp/ON (R_{HAp}; see discussion above) remains equal. For this reason, we attribute this behaviour to the steric effects caused by the reorientation of the OH$^-$ groups in p-HAp (Fig. 1a). Note that such steric effects on the OH$^-$ columns were previously studied as part of the stability and transition mechanisms between the different HAp polymorphs.[30]

Overall, several competing structural and electronic features in the p-HAp samples have been determined to influence the NTP treatment, including the optimum atmospheres to be used. Further explorations of such effects are currently under study because, while the potential of combining both techniques is clearly sketched, no precise conclusions can be extracted on this topic from the present results.

3.5 Catalytic benchmarking of HPPD hydroxyapatite-based composites

The exceptional electrical responses obtained through HPPD for s-HAp NTP treated samples render them as suitable catalyst candidates for CO_2 capture and conversion reactions. As stated in the SI, batch reactions were carried out under mild conditions (6 bar of CO_2 and 150 °C and 40 mL of water) employing s-HAp, s-HAp/O, p-HAp and p-HAp/O as catalysts. The yields achieved were normalized by catalyst weight (g_c). The obtained yields and selectivities are displayed in Fig. 6a and Table S6, respectively, while the products identification through ^{1}H-NMR is displayed in Fig. 6b. The total product yield detected in the supernatant (*i.e.* water collected after the reaction, corresponding to the products desorbed from the catalyst) reached 537.85 ± 3.40 μmol g_c^{-1} for s-HAp/O, representing a 230% increase with respect to the non-doped version. This result is consistent with the improvement detected in electrochemical response discussed in the Fig. 2 and Table 1 (Section 3.2), enabling HPPD to be established as an excellent method for oxygen doping s-HAp. According to the lower impedance deviations observed in Fig. 5a, p-HAp and p-HAp/O present highly similar yields, 351.80 ± 11.76 and 330.09 ± 8.51 μmol g_c^{-1}, respectively, which is an expected result due to the impossibility of oxygen diffusion for p-HAp doping. Interestingly, although s-HAp/O shows slightly lower electrochemical conductivity compared to p-HAp, its catalytic activity is higher. Such a feature is attributed to the fact that oxygen dopants could also act as binding sites, tuning the kinetics of the reaction. Nevertheless, this result does not demerit p-HAp as it has been specifically designed to present catalytic plasticity properties (*i.e.* the selectivity of the catalyst can be controlled)[59] through the presence of the brushite surface layer. Indeed, concerning the selectivity, as reported by Sans *et al.*,[59] a brushite surface layer on p-HAp promotes longer carbon chain products. However, the oxygen-doped brushite on p-HAp/O interferes with this behavior, resulting in the promotion of C1 products (Table S6). On the other hand, the selectivity of s-HAp/O and s-HAp are similar, promoting the formation of C1 products, with formic acid being selectivity boosted up to 50%. Anyhow, this is a surprising result as there are no other strategies (*i.e.*, only HPPD and TSP, as considered in this work) to produce HAp catalysts capable of successfully performing such CO_2-conversion reactions under mild conditions. Finally, in order to assess s-HAp/O stability, EIS measurements were performed before and after a catalytic reaction (Fig. S12). Almost identical Nyquist curves were achieved, thus proving that the oxygen doping was permanent and that the samples might be reused.

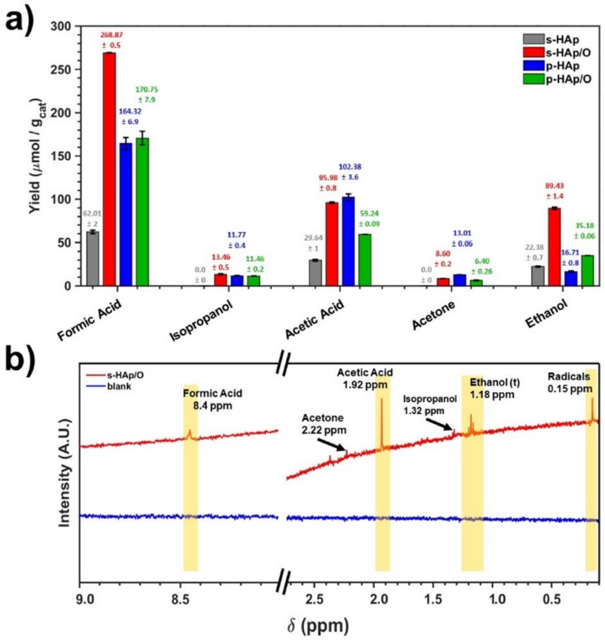

Fig. 6 (a) Catalytic yields of products detected in the supernatant for different tested catalysts. (b) ^{1}H-NMR spectra with labelled reaction products for the s-HAp/O and a blank (no catalyst) reaction.

The HPPD effectiveness for enhancing the catalytic yield of s-HAp encouraged the authors to perform a literature mini-review concerning state-of-the-art catalysts modified by means of plasma doping,[60–67] as detailed in the Experimental methods section. For this purpose, Fig. 7 was assembled comparing recently published works in terms of plasma treatment energy required *versus* percentage of doping replacement achieved (listed in Table S7). As observed, with a minimal amount of energy, the HPPD presented in this work accomplishes the highest percentage of doping replacement. In addition, other chemical doping strategies for HAp are also documented in Table 4, aiming to give a comprehensive view of the differences with respect to HPPD. The majority of doping techniques are time-expensive and require solvents, rendering HPPD highly advantageous compared to these other approaches. Despite this, chemical methods offer vast tunability, enabling high degrees of precision when it comes to the selection of dopant types or molar ratio substitution. As mentioned, the NTP effects on samples are regulated by low-energy collisions, resulting in low doping rates. However, combining vacancy-engineering with NTP doping, the energetic requirements for atomic substitution are vastly lowered, leading to an extremely interesting approach for precise nanoscale doping of materials and a highly promising alternative to conventional doping

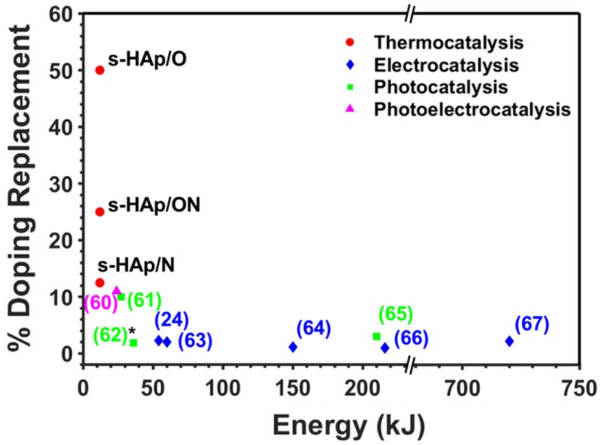

Fig. 7 Comparative plot with different state-of-the-art catalysts designed through plasma doping. Red points represent samples reported in this work (*i.e.* s-HAp/O, s-HAp/ON, and s-HAp/N). Details on axis assignments can be found in the Experimental methods section. Details of each reference can be found in Table S7. Study 3 (marked with an asterisk) did not specify a precise amount of plasma processing time; hence, the authors have assumed an arbitrary energy.

Table 4 Strategies reported for chemically doping HAp

Doping %	Replacement %	Dopant	Doping method	Time	Catalysis type	Ref.
0.6–13.6	4.2–100	V	Coprecipitation	17 h	Thermocatalysis	68
0.3–5.0	1.4–22.0	Cu	Wet chemical precipitation	>1 day	Photocatalysis	69
—	0.0–30.0	Fe	Hydrothermal synthesis	>1 day	Photocatalysis	37
—	5.0–20.0	Co	Coprecipitation	15 h	Photothermal catalysis	38
—	18.6	Fe	Aqueous mixing + calcination	30 min	Photocatalysis	70
23.4	—	CeO_2	Coprecipitation	>1 day	Thermocatalysis	39
~0.2	—	ZnO, TiO_2	Aqueous mixing + calcination	1 h to <1 day	Photocatalytic degradation	71
—	0.3–2.1	Al	Hydrothermal	>1 day	Catalytic degradation	72
—	1.0–20.0	Co	Hydrothermal	>1 day	Catalytic degradation	73

procedures. It must be emphasized that, although in this work oxygen-doped s-HAp through NTP provided impressive results, this treatment might have constrained applications. Indeed, different types of lattice vacancies can be generated in a vast range of materials. However, achieving channelled diffusion of ions while maintaining the material's structural stability, and determining suitable dopant candidates, might be challenging, restraining bulk doping, as seen for the p-HAp case. Nonetheless, the successful extension of the TSP treatment to binary oxides[74] and polymeric materials[75] offers a promising alternative pathway to the design of HPPD candidate materials. Through re-crystallization and/or generation of crystal lattice distortions, which are key parameters for achieving HPPD (as reported in this work), alternative diffusion mechanisms could be achieved without compromising the material's stability. Overall, the range of HPPD applications demonstrates a strong potential, motivating further explorations of specific materials to extend the method and assess the feasibility of the approach from a general point of view.

4. Conclusions

In the present work, a high-performing plasma doping (HPPD) strategy consisting of combining vacancy-engineering with non-thermal plasma (NTP) has been introduced as a promising method for doping HAp, being a fast, sustainable and solvent-free technique. Vacancy-engineered HAp disks were prepared and treated with NTP under different atmospheres (100% O_2, 50/50% O_2/N_2, and 100% N_2), resulting in remarkably improved electrical responses for the bulk material in all cases, while maintaining HAp structural stability. For s-HAp/O samples, 5.62% oxygen dopant surface loading was achieved, yielding ~50% doping replacement efficiency. Furthermore, although bulk doping quantification has not been assessed, bulk doping processes were elucidated through DFT calculations. Accordingly, the diffusion of oxygen ions through the OH^- columns present in HAp would be promoted through a potential difference generated between the neutral gas regime in the NTP and the HAp vacancies, as observed through NEB and ELF studies. In addition, HPPD was tested for p-HAp, leading to less favourable electrical responses than observed for s-HAp samples due to oxygen doping of the hydroxyl-stabilized brushite surface layer. Finally, catalytic benchmarking for s-HAp, p-HAp and their respective NTP 100% O_2 treated counterparts was determined. More specifically, the catalytic activity of the samples was tested through their capacity to convert CO_2 into valuable C1–C2 products (*e.g.*, formic acid and ethanol, among others) under mild conditions. While p-HAp samples treated with any O_2 plasma gas content did not present significant changes, an impressive 230% boost in the catalytic yield was obtained for s-HAp/O with respect to s-HAp. Therefore, HPPD is established as an energy-efficient doping strategy for HAp catalysts, enabling the harnessing of NTP's maximum potential, offering an alternative to conventional chemical doping methods. Although HAp is presented as an ideal case example for HPPD, this strategy is not restricted to calcium phosphate salts. As discussed, combining lattice engineering (*e.g.*, generation of vacancies or specific lattice ordinations by means of TSP treatment to control atomic diffusion processes) with non-thermal plasma also has great potential for binary oxides or polymeric materials. Thus, the mechanisms and synergies behind HPPD are presented as a generalized novel approach for highly efficient doping that can go beyond the HAp case.

Conflicts of interest

Authors declare that the preparation and application of permanently polarized hydroxyapatite as a catalyst was patented by the Universitat Politècnica de Catalunya and B. Braun Surgical S.A.U. (EP16382381, EP16382524, P27990EP00, PCT/EP2017/069437, P58656 EP, P59205 EP, P59091 EP, P59008 EP, P59528 EP, 2021P00074 EP, P59985 EP).

Data availability

The data supporting this article have been included as part of the supplementary information (SI). Supplementary information is available. See DOI: **https://doi.org/10.1039/d5ta06860f**.

Acknowledgements

This publication and other research outcomes are supported by the predoctoral program AGAUR-FI ajuts (2023 FI-100056) Joan Oró, which is backed by the Secretariat of Universities and Research of the Department of Research and Universities of the Generalitat of Catalonia, as well as the European Social Plus Fund. The authors acknowledge the Agència de Gestió d'Ajuts

Universitaris i de Recerca (2021 SGR 003879). This work is part of Maria de Maeztu Units of Excellence Programme CEX2023-001300-M/funded by MCIN/AEI/10.13039/501100011033. Support for the research of C. A. was also received through the prize "ICREA Academia" for excellence in research funded by the Generalitat de Catalunya.

Notes and references

1 M. Malekzadeh and M. T. Swihart, *Chem. Soc. Rev.*, 2021, **50**, 7132–7249.

2 S. K. B. C. Panda, K. Sen and S. Mukhopadhyay, *J. Cleaner Prod.*, 2021, **329**, 129725.

3 L. Di, J. Zhang, X. Zhang, H. Wang, H. Li, Y. Li and D. Bu, *J. Phys. D: Appl. Phys.*, 2021, **54**, 333001.

4 C. M. Laureano-Anzaldo, M. E. González-López, A. A. Pérez-Fonseca, L. E. Cruz-Barba and J. R. Robledo-Ortíz, *Carbohydr. Polym.*, 2021, **252**, 117195.

5 X. Chen, C. Wang, Y. Zhao, Y. Wang, X. Yin and N. Zhang, *J. Mater. Chem. A*, 2024, **12**, 31797–31817.

6 J. He, X. Wen, L. Wu, H. Chen, J. Hu and X. Hou, *TrAC, Trends Anal. Chem.*, 2022, **156**, 116715.

7 G. K. Dalapati, H. Sharma, A. Guchhait, N. Chakrabarty, P. Bamola, Q. Liu, G. Saianand, A. M. Sai Krishna, S. Mukhopadhyay, A. Dey, T. K. S. Wong, S. Zhuk, S. Ghosh, S. Chakrabortty, C. Mahata, S. Biring, A. Kumar, C. S. Ribeiro, S. Ramakrishna, A. K. Chakraborty, S. Krishnamurthy, P. Sonar and M. Sharma, *J. Mater. Chem. A*, 2021, **9**, 16621–16684.

8 A. Bogaerts, X. Tu, J. C. Whitehead, G. Centi, L. Lefferts, O. Guaitella, F. Azzolina-Jury, H.-H. Kim, A. B. Murphy, W. F. Schneider, T. Nozaki, J. C. Hicks, A. Rousseau, F. Thevenet, A. Khacef and M. Carreon, *J. Phys. D: Appl. Phys.*, 2020, **53**, 443001.

9 A. H. Khoja, A. Mazhar, F. Saleem, M. T. Mehran, S. R. Naqvi, M. Anwar, S. Shakir, N. A. Saidina Amin and M. B. Sajid, *Int. J. Hydrogen Energy*, 2021, **46**, 15367–15388.

10 Z. Ye, L. Zhao, A. Nikiforov, J.-M. Giraudon, Y. Chen, J. Wang and X. Tu, *Adv. Colloid Interface Sci.*, 2022, **308**, 102755.

11 X. Liu, W. Chen, C. Zhang, T. Li, J. Huang, G. Chen, T. Shao, T. Gong and K. Ostrikov, *ACS Sustainable Chem. Eng.*, 2022, **10**, 8064–8074.

12 Q. Zhang, S. Tao, J. Du, A. He, Y. Yang and C. Tao, *J. Mater. Chem. A*, 2020, **8**, 8410–8420.

13 K. Li, Y. de Rancourt de Mimérand, X. Jin, J. Yi and J. Guo, *ACS Appl. Nano Mater.*, 2020, **3**, 2830–2845.

14 Y. Guo, C. Zhang, Y. Wu, H. Yu, S. Zhang, A. Du, K. (Ken) Ostrikov, J. Zheng and X. Li, *J. Mater. Chem. A*, 2020, **8**, 10402–10408.

15 J. Zhang, X. Zhang, C. Shi, X. Yu, Y. Zhou and L. Di, *Small*, 2024, **20**, 2406767.

16 Y.-C. Li, X.-S. Li, J.-L. Liu, B. Zhu, G. Zhang, D. Liu, W. Liu, X. Guo and A.-M. Zhu, *ACS Catal.*, 2025, **15**, 1027–1037.

17 W. Ding, S. Yuan, Y. Yang, X. Li and M. Luo, *J. Mater. Chem. A*, 2023, **11**, 23653–23682.

18 A. Kumar and V. Krishnan, *Adv. Funct. Mater.*, 2021, **31**, 2009807.

19 S. R. Ede and Z. Luo, *J. Mater. Chem. A*, 2021, **9**, 20131–20163.

20 Y. Jia, Y. Zhang, H. Xu, J. Li, M. Gao and X. Yang, *ACS Catal.*, 2024, **14**, 4601–4637.

21 J. Zhang, Y. Hua, H. Li, X. Zhang, C. Shi, Y. Li, L. Di and Z. Wang, *Chem. Eng. J.*, 2023, **478**, 147288.

22 S. Guo, J. Zhang, G. Fan, A. Shen, X. Wang, Y. Guo, J. Ding, C. Han, X. Gu and L. Wu, *Angew. Chem., Int. Ed.*, 2024, **63**, e202409698.

23 J. Li, Y. Zhou, W. Tang, J. Zheng, X. Gao, N. Wang, X. Chen, M. Wei, X. Xiao and W. Chu, *Appl. Catal., B*, 2021, **285**, 119861.

24 Y. Wang, F. Yu, M. Zhu, C. Ma, D. Zhao, C. Wang, A. Zhou, B. Dai, J. Ji and X. Guo, *J. Mater. Chem. A*, 2018, **6**, 2011–2017.

25 T. H. Nguyen, D. Yang, B. Zhu, H. Lin, T. Ma and B. Jia, *J. Mater. Chem. A*, 2021, **9**, 7366–7395.

26 R. Sreena, G. Raman, G. Manivasagam and A. J. Nathanael, *J. Mater. Chem. B*, 2024, **12**, 11278–11301.

27 M. d. Kawsar, M. d. Sahadat Hossain, M. d. K. Alam, N. M. Bahadur, M. d. A. A. Shaikh and S. Ahmed, *J. Mater. Chem. B*, 2024, **12**, 3376–3391.

28 Z. Xiong, Y. Zhu, Z. Wang, Y. Chen and H. Yu, *Adv. Funct. Mater.*, 2022, **32**, 2106978.

29 M. He, Z. Zhang, M. Wang, C. Liang, H. Wang, C. Cheng, Y. Li, Y. Wang and Z. Zhang, *J. Hazard. Mater.*, 2025, **481**, 136525.

30 J. Sans, M. Arnau, P. Turon and C. Alemán, *Mater. Horiz.*, 2022, **9**, 1566–1576.

31 Z. Boukha, J. R. González-Velasco and M. A. Gutiérrez-Ortiz, *Appl. Catal., B*, 2020, **270**, 118851.

32 J. Guo, P. N. Duchesne, L. Wang, R. Song, M. Xia, U. Ulmer, W. Sun, Y. Dong, J. Y. Y. Loh, N. P. Kherani, J. Du, B. Zhu, W. Huang, S. Zhang and G. A. Ozin, *ACS Catal.*, 2020, **10**, 13668–13681.

33 H. Yook, J. Hwang, W. Yeo, J. Bang, J. Kim, T. Y. Kim, J. Choi and J. W. Han, *Adv. Mater.*, 2023, **35**, 2204938.

34 B.-C. Zhou, W.-C. Li, W.-L. Lv, S.-Y. Xiang, X.-Q. Gao and A.-H. Lu, *ACS Catal.*, 2022, **12**, 12045–12054.

35 M. Arnau, P. Turon, C. Alemán and J. Sans, *J. Mater. Chem. A*, 2023, **11**, 1324–1334.

36 H. Martínez-Hernández, J. A. Mendoza-Nieto, H. Pfeiffer, J. Ortiz-Landeros and L. Téllez-Jurado, *Chem. Eng. J.*, 2020, **401**, 125992.

37 K. Shu, C. Chuaicham, Y. Noguchi, L. Xu and K. Sasaki, *Chem. Eng. J.*, 2023, **459**, 141474.

38 Y. Peng, H. Szalad, P. Nikacevic, G. Gorni, S. Goberna, L. Simonelli, J. Albero, N. López and H. García, *Appl. Catal., B*, 2023, **333**, 122790.

39 G. Lin, H. Fan, Y. Zhan, C. Chen, X. Zhao, W. Lin, B. Li, J. Wang, J. Li, W. Song and J. Fu, *ACS Catal.*, 2024, **14**, 1862–1873.

40 M. Miyauchi, T. Watanabe, D. Hoshi and T. Ohba, *Dalton Trans.*, 2019, **48**, 17507–17515.

41 S. S. Bhat, U. V. Waghmare and U. Ramamurty, *Cryst. Growth Des.*, 2014, **14**, 3131–3141.

42 H. Brasil, A. F. B. Bittencourt, K. C. E. S. Yokoo, P. C. D. Mendes, L. G. Verga, K. F. Andriani, R. Landers,

J. L. F. Da Silva and G. P. Valença, *J. Catal.*, 2021, **404**, 802–813.

43 Y. Miao, W. Tian, J. Han, N. Li, D. Chen, Q. Xu and J. Lu, *Nano Energy*, 2022, **100**, 107473.

44 X. Song, F. Zhou, H. Ma, Y. Liu and G. Wu, *ChemCatChem*, 2023, **15**, e202300785.

45 J. Tian, Y. Fan, T. Wei, Q. Guo, W. Fang, Y. Cong, D. Zhang and Y. Guo, *Catal. Sci. Technol.*, 2025, **15**, 1958–1971.

46 T. Eknapakul, S. Kuimalee, W. Sailuam, S. Daengsakul, N. Tanapongpisit, P. Laohana, W. Saenrang, A. Bootchanont, A. Khamkongkaeo and R. Yimnirun, *RSC Adv.*, 2024, **14**, 4614–4622.

47 C. Lv, P. Jiao, H. Xin, L. Wu, G. Ouyang and X. Hou, *Appl. Catal., B*, 2024, **340**, 123248.

48 J. Sans, M. Arnau, F. Estrany, P. Turon and C. Alemán, *Adv. Materials. Inter.*, 2021, **8**(11), 2100163.

49 J. Sans, M. Arnau, V. Sanz, P. Turon and C. Alemán, *Adv. Materials. Inter.*, 2022, **9**(5), 2101631.

50 B. Mahns, F. Roth and M. Knupfer, *J. Chem. Phys.*, 2012, **136**, 134503.

51 J. He, Y. Wen, D. Han, P. Zeng, P. Zheng, L. Zheng, W. Su, Z. Wu and Y. Zhang, *Mater. Sci. Semicond. Process.*, 2023, **158**, 107347.

52 D. N. G. Krishna and J. Philip, *Appl. Surf. Sci. Adv.*, 2022, **12**, 100332.

53 M. Arnau, L. Pielsticker, W. Hetaba, J. Casanovas, P. Turon, C. Alemán and J. Sans, *ACS Catal.*, 2025, 11150–11162.

54 T. R. Gengenbach, G. H. Major, M. R. Linford and C. D. Easton, *J. Vac. Sci. Technol., A*, 2021, **39**, 013204.

55 F. Ruiz, Z. Benzo, Á. Garaboto, J. Salas and J. L. Brito, *J. Anal. At. Spectrom.*, 2022, **37**, 668–676.

56 U. R. Kortshagen, R. M. Sankaran, R. N. Pereira, S. L. Girshick, J. J. Wu and E. S. Aydil, *Chem. Rev.*, 2016, **116**, 11061–11127.

57 M. A. Lieberman and A. J. Lichtenberg, *Principles of Plasma Discharges and Materials Processing*, 2005.

58 M. Arnau, J. Sans, J. L. Tamarit, M. Romanini, P. Turon and C. Alemán, *Adv. Mater. Interfaces*, 2024, **11**(33), 2400422.

59 J. Sans, M. Arnau, V. Sanz, P. Turon and C. Alemán, *Chem. Eng. J.*, 2022, **433**, 133512.

60 S. Y. Lee, Y. J. Lee, I.-H. Yoo, H. W. Kim, H. Song, S. W. Heo, S. S. Kalanur, G. Mohapatra, Rohma, H. Ko and H. Seo, *Appl. Surf. Sci.*, 2024, **652**, 159213.

61 W. Zhao, S. Liu, S. Zhang, R. Wang and K. Wang, *Catal. Today*, 2019, **337**, 37–43.

62 P. Gholami, A. Khataee, A. Bhatnagar and B. Vahid, *ACS Appl. Mater. Interfaces*, 2021, **13**, 13072–13086.

63 Y. Shen, L. Qian, Q. Xu, S. Wang, Y. Chen, H. Lu, Y. Zhou, J. Ye, J. Zhao, X. Gao and S. Zhang, *J. Environ. Sci.*, 2025, **150**, 246–253.

64 Y. Li, Y. Wan, J. Yao, H. Zheng, X. Wang, X. Liu, B. Ouyang, C. Huang, K. Deng and E. Kan, *Phys. Chem. Chem. Phys.*, 2023, **25**, 31628–31635.

65 Y. Tan, L. Sun, G. Wang, R. Zhang, J. Hou, R. Zhang and W. Zhao, *J. Cleaner Prod.*, 2022, **370**, 133507.

66 K. Chen, S. Kim, R. Rajendiran, K. Prabakar, G. Li, Z. Shi, C. Jeong, J. Kang and O. L. Li, *J. Colloid Interface Sci.*, 2021, **582**, 977–990.

67 H. Fan, W. Chen, G. Chen, J. Huang, C. Song, Y. Du, C. Li and K. (Ken) Ostrikov, *Appl. Catal., B*, 2020, **268**, 118440.

68 R. D. Patria, R. Kumar, L. Luo, S. Varjani, J. W. C. Wong and J. Zhao, *ACS Sustainable Chem. Eng.*, 2022, **10**, 10514–10525.

69 Md. S. Hossain, S. M. Tuntun, N. M. Bahadur and S. Ahmed, *RSC Adv.*, 2022, **12**, 34080–34094.

70 K. Shu, C. Chuaicham and K. Sasaki, *Chem. Eng. J.*, 2023, **477**, 146994.

71 M. d. Kawsar, M. d. Sahadat Hossain, S. Tabassum, N. M. Bahadur and S. Ahmed, *RSC Adv.*, 2024, **14**, 11570–11583.

72 Y. Sun, X. Wei, S. Wu, F. Liu, B. Liu and W. Han, *Appl. Catal., A*, 2025, **691**, 120089.

73 L. Wang, Y. Ruan, Z. Diao, D. Chen and L. Kong, *Environ. Res.*, 2025, **267**, 120657.

74 J. Sans, M. Arnau, A. Fontana-Escartín, P. Turon and C. Alemán, *Chem. Mater.*, 2023, **35**, 3765–3780.

75 M. Gul, A. Fontana-Escartín, M. Arnau, J. Sans, S. Lanzalaco, E. Armelin, E. Chiesa, I. Genta, M. M. Pérez-Madrigal and C. Alemán, *ACS Appl. Polym. Mater.*, 2024, **6**, 15070–15081.